

Parametric Solitons in Two-Dimensional Lattices of Purely Nonlinear Origin

Katia Gallo

Optoelectronics Research Centre, University of Southampton, SO17 1BJ Southampton, United Kingdom

Alessia Pasquazi, Salvatore Stivala, and Gaetano Assanto*

Nonlinear Optics and Optoelectronics Lab (NooEL), University "Roma Tre," Via della Vasca Navale 84, 00146 Rome, Italy

(Received 5 July 2007; published 6 February 2008)

We demonstrate spatial solitons via twin-beam second-harmonic generation in hexagonal lattices realized by poling lithium niobate planar waveguides. These solitons can be steered by acting on power, direction, and wavelength of the fundamental frequency input.

DOI: 10.1103/PhysRevLett.100.053901

PACS numbers: 42.65.Tg, 42.65.Ky

Nonlinear physics in periodic lattices is rich and fascinating in several branches, from biology [1] to solid state physics [2], ferromagnetism [3], and Bose-Einstein condensates [4]. In optics, spatial solitons (SS), i.e., self-guiding light filaments, are one of the most intriguing outcomes of nonlinearity [5,6] and a frontier in periodic systems [7]. SS in media with periodically structured linear properties have been intensely investigated [8–12], but only recently in higher dimensionality (2D) lattices [13,14]. Previous studies have dealt with photonic crystals and Kerr-like nonlinearities [15], photorefractive media [8], and Bose-Einstein condensates [16].

Another scenario for nonlinear waves in periodic structures has been enlightened by quasi phase matching (QPM) [17] in quadratic crystals such as LiNbO₃ [18], which can create purely nonlinear photonic lattices (NPL) where, rather than the linear $\chi^{(1)}$, the quadratic $\chi^{(2)}$ susceptibility is periodically modulated in 1D [17,18] or 2D [19,20]. A quadratic response can sustain multicolor SS (or similtions) [21] through parametric generation and amplification that counteract diffractive beam spreading [22]. Nearly a decade ago, mutual trapping and spatial locking of multifrequency components into similtions were demonstrated in uniform $\chi^{(2)}$ media [23], confirming the predictions in Ref. [24]. The study of $\chi^{(2)}$ solitons has largely progressed [25], including 1D QPM gratings [26].

Hereby we report for the first time spatial similtions in two-dimensional quadratically nonlinear lattices. With reference to SS via twin-beam second-harmonic generation (TB SHG) [27], we demonstrate their enhanced wavelength-dependent and spatial features stemming from the higher dimensionality NPL.

Figure 1(a) illustrates our 2D NPL structure. A 2D sign-modulated distribution of the quadratic susceptibility $\chi^{(2)}$ is achieved by electric field poling [18] on a z -cut 500 μm thick congruent LiNbO₃ crystal. The 2D lattice consists of an $8 \times 18 \text{ mm}^2$ hexagonal array (HexLN) of ferroelectric domains with reversed polarity and period $\Lambda = 16.4 \mu\text{m}$ [Fig. 1(b)]. A planar waveguide for light confinement along z is subsequently embedded in the 2D NPL by the fabrication sequence of proton exchange in pure benzoic

acid (29 h at 170 °C), thermal annealing (13 h at 200 °C and 7 h at 330 °C), and, finally, reverse proton exchange in a LiNO₃:NaNO₃:KNO₃ eutectic melt (28 h at 320 °C) [27]. Such a waveguide is optimized for efficient guided-wave TB SHG from 1530–1650 nm where it supports only the TM₀ eigenmode. The planar configuration leaves unaffected the in-plane degrees of freedom of the 2D lattice while significantly enhancing the SHG efficiency, the latter playing a key role in lowering the required soliton power. Figure 1(c) sketches TB SHG: a fundamental frequency (FF) pump at $\lambda_\omega \sim 1550 \text{ nm}$, propagating at a small angle (θ_ω) with respect to the symmetry axis (Σ) of the planar NPL, excites two SHG resonances with outputs SH⁽⁺⁾ and SH⁽⁻⁾. Efficient SHG occurs as momentum conservation (i.e., quasi phase matching) is granted by the NPL via two of its lowest-order reciprocal lattice vectors $\mathbf{G}^{(+)}$ and $\mathbf{G}^{(-)}$

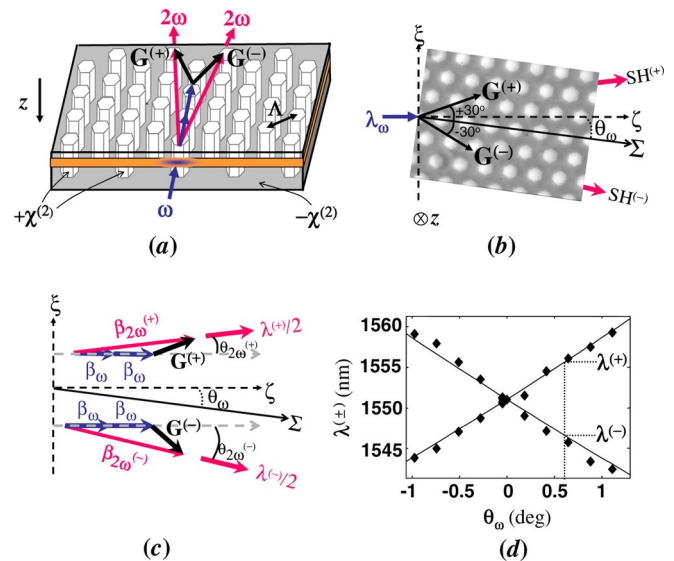


FIG. 1 (color online). (a) Sketch of a HexLN planar waveguide. (b) TB SHG geometry (top view, $-z$ face). (c) QPM diagram in the ξ - ζ plane. (d) SHG resonant wavelengths [$\lambda^{(\pm)}$] versus FF incidence angle θ_ω : measurements (diamonds) and linear fits (solid lines). The dotted lines indicate phase matching for $\theta_\omega = 0.58^\circ$, as discussed in Fig. 3.

at $\pm 30^\circ$ with respect to Σ , respectively, with $|\mathbf{G}^{(+)}| = |\mathbf{G}^{(-)}| = 4\pi/(\Lambda\sqrt{3})$. For the two noncollinear SHG processes $\text{FF} + \text{FF} \rightarrow \text{SH}^{(+)}$ and $\text{FF} + \text{FF} \rightarrow \text{SH}^{(-)}$ the QPM conditions take the vectorial form [Fig. 1(c)]:

$$\Delta \boldsymbol{\beta}^{(+)} = 2\boldsymbol{\beta}_\omega - \boldsymbol{\beta}_{2\omega}^{(+)} + \mathbf{G}^{(+)} = \mathbf{0} \quad (1)$$

$$\Delta \boldsymbol{\beta}^{(-)} = 2\boldsymbol{\beta}_\omega - \boldsymbol{\beta}_{2\omega}^{(-)} + \mathbf{G}^{(-)} = \mathbf{0}, \quad (2)$$

$\boldsymbol{\beta}_\omega$, $\boldsymbol{\beta}_{2\omega}^{(+)}$, and $\boldsymbol{\beta}_{2\omega}^{(-)}$ being the wave vectors for FF, $\text{SH}^{(+)}$, and $\text{SH}^{(-)}$ TM_0 modes, respectively. In a frame of reference with axis $\hat{\boldsymbol{\xi}} = \boldsymbol{\beta}_\omega/|\boldsymbol{\beta}_\omega|$ parallel to the FF launch direction and an orthogonal axis $\hat{\boldsymbol{\zeta}} \perp \hat{\boldsymbol{\xi}}$ [Fig. 1(c)], Eqs. (1) and (2) can be reduced to the scalar form:

$$\Delta \beta_\zeta^{(\pm)} = 2|\boldsymbol{\beta}_\omega| - |\boldsymbol{\beta}_{2\omega}^{(\pm)}| \cos\theta_{2\omega}^{(\pm)} + |\mathbf{G}^{(\pm)}| \cos(\pi/6 \mp \theta_\omega) = 0 \quad (3)$$

$$\Delta \beta_\xi^{(\pm)} = 2|\boldsymbol{\beta}_\omega| - |\boldsymbol{\beta}_{2\omega}^{(\pm)}| \sin\theta_{2\omega}^{(\pm)} + |\mathbf{G}^{(\pm)}| \sin(\pi/6 \mp \theta_\omega) = 0, \quad (4)$$

where $\theta_{2\omega}^{(\pm)}$ are the angles between $\boldsymbol{\beta}_{2\omega}^{(\pm)}$ and $\boldsymbol{\beta}_\omega$. For a given FF incidence angle θ_ω , the above identify two SHG resonant wavelengths $\lambda^{(+)}$ and $\lambda^{(-)}$ for $\text{FF} + \text{FF} \rightarrow \text{SH}^{(+)}$ and $\text{FF} + \text{FF} \rightarrow \text{SH}^{(-)}$, respectively. Their wavelength separation can be adjusted from zero, i.e., $\lambda^{(+)} = \lambda^{(-)} = \lambda_0$ (symmetric TB SHG, $\theta_\omega = 0^\circ$), to several nm just by varying the FF angle of propagation, as shown in Fig. 1(d).

The mismatches $\Delta \beta_\zeta^{(\pm)}$ and $\Delta \beta_\xi^{(\pm)}$ depend on both the wavelength (λ_ω) and the propagation angle (θ_ω) of the FF pump. The Ewald sphere constructions [19] with $|\theta_\omega| < 3^\circ$ and $\lambda_\omega \in (1530\text{--}1650)$ nm indicate that $|\Delta \boldsymbol{\beta}^{(\pm)}| = \Delta \beta^{(\pm)} \cong \Delta \beta_\zeta^{(\pm)}$, with $\theta_{2\omega}^{(\pm)} \cong \pm 0.012$ rad. By combining interpolation of QPM data in Fig. 1(d) with the calculated TM_0 -mode dispersion, we obtain the empirical dependence $\Delta \beta^{(\pm)}|_{\text{cm}^{-1}} = 1.54\pi(\lambda_\omega - \lambda_0)|_{\text{nm}} \mp 12.3\pi\theta_\omega|_{\text{deg}}$, with λ_0 the resonant value for symmetric TB SHG ($\theta_\omega = 0^\circ$). Neglecting higher-order resonances, the (equal) nonlinear strengths associated with $\mathbf{G}^{(+)}$ and $\mathbf{G}^{(-)}$ can be derived via a 2D Fourier analysis of perfect hexagonal lattices:

$$\Gamma = \left(\frac{3}{\pi^2} d_{33}\right) \frac{2\omega^2}{c^2} \sqrt{\frac{\omega\mu_0}{\beta_\omega^2 \beta_{2\omega} h_{\text{eff}}}}, \quad (5)$$

with d_{33} the nonlinear tensor element, μ_0 the magnetic permeability, c the speed of light in vacuum, and $h_{\text{eff}} = 3.2 \mu\text{m}$ the effective SHG depth.

To gain insight into parametric wave dynamics, first we analyze wave propagation in the planar NPL. To this extent we model TB SHG in $(1+1)D$ with a set of coupled mode equations for the slowly varying envelopes A and $B^{(\pm)}$ for FF and $\text{SH}^{(\pm)}$ waves, respectively:

$$\frac{\partial A}{\partial \zeta} + i\sigma_\omega \frac{\partial^2 A}{\partial \xi^2} = -i\gamma^+ A^* B^+ - i\gamma^- A^* B^-$$

$$\frac{\partial B^+}{\partial \zeta} + \rho_{2\omega}^+ \frac{\partial B^+}{\partial \xi} + i\sigma_{2\omega}^+ \frac{\partial^2 B^+}{\partial \xi^2} - i\delta\beta^+ B^+ = -i\gamma^+ A^2 \quad (6)$$

$$\frac{\partial B^-}{\partial \zeta} + \rho_{2\omega}^- \frac{\partial B^-}{\partial \xi} + i\sigma_{2\omega}^- \frac{\partial^2 B^-}{\partial \xi^2} - i\delta\beta^- B^- = -i\gamma^- A^2.$$

Transverse and longitudinal coordinates ξ and ζ [Figs. 1(b) and 1(c)] are normalized to the input beam waist (w_0) and diffraction length $L_D = \beta_\omega w_0^2/2$, respectively. Equations (6) are integrated with a split-step beam propagator in the FF-pulse frame of reference, using a Gaussian transverse distribution of the FF input $A(\xi, \zeta = 0) = \exp(-\xi^2)$ and scaling the field envelopes to the square root of the FF power P_0 (for pulsed excitations $P(t) = P_0 w_0 (\pi/2)^{+1/2} \times \exp[-(t/\tau)^2]$). We adopt a quasistationary—cw pointwise—approach, appropriate to our experimental conditions where temporal walk-off can be neglected. Equations (6) account for in-plane angular deviation of the $\text{SH}^{(\pm)}$ beams [$\rho_{2\omega}^{(\pm)} = \theta_{2\omega}^{(\pm)} L_D/w_0 \sim \pm 1.5$], as well as diffraction at FF and SH [$\sigma_\omega = L_D/(2\beta_\omega w_0^2) = 1/4$ and $\sigma_{2\omega}^{(\pm)} = L_D/(2\beta_{2\omega} w_0^2) \sim 1/8$]. The normalized mismatches $\delta\beta^{(\pm)} \equiv \Delta \beta^{(\pm)} L_D$ and nonlinear coupling $\gamma^{(\pm)} \equiv \Gamma L_D \sqrt{P_0}$ define a parameter space wider than conventional SHG.

Let us first consider symmetric TB SHG, where $\theta_\omega = 0$ and $\delta\beta^{(+)} \equiv \delta\beta^{(-)}$. Figures 2(a) and 2(b) display the evolution of FF and SH in the plane $\{\xi - \zeta\}$ for propagation over six diffraction lengths at low ($\gamma^{(\pm)} = 0.01$) and high ($\gamma^{(\pm)} = 5.0$) excitations, respectively, for $\delta\beta^{(+)} = \delta\beta^{(-)} = 5\pi$. In the linear regime [Fig. 2(a)] the FF diffracts in ξ , whereas the SH flows preferentially along the two directions determined by QPM [Eqs. (1) and (2) and Fig. 1(c)]. At high excitations [Fig. 2(b)] the parametric exchange between FF and SH leads to mutual trapping and

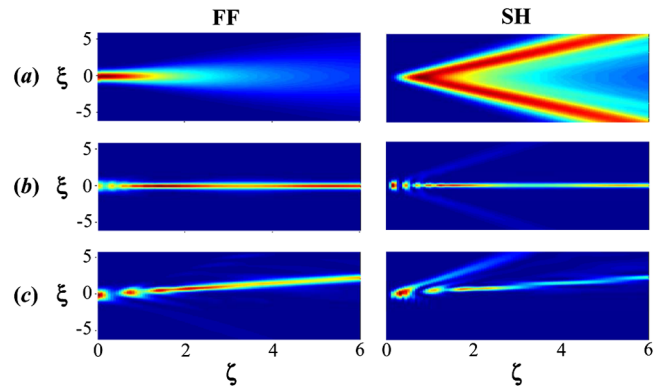


FIG. 2 (color online). Simulated TB SHG with continuous-wave input. FF and SH propagation for (a) $\delta\beta^{(+)} = \delta\beta^{(-)} = 5\pi$, $\gamma^{(\pm)} = 0.01$; (b) $\delta\beta^{(+)} = \delta\beta^{(-)} = 5\pi$, $\gamma^{(\pm)} = 5$; (c) $\delta\beta^{(-)} = -20\pi$, $\delta\beta^{(+)} = \pi$, $\gamma^{(\pm)} = 5$.

locking into a soliton. The cascading signature of parametric solitons can be recognized in the oscillations in the early stages of propagation [22]. Each of the two noncollinear SHG processes tends to confine the FF into a “walking soliton” with a net angular deviation ($\rho_{2\omega}^{(\pm)}$) toward the corresponding SH wave vector $\beta_{2\omega}^{(\pm)}$ [28–30]; as the two symmetric SHG pulling actions balance each other, the ultimate result is a two-color SS propagating along the initial FF direction ($\xi = 0$). The analysis versus detuning shows that solitons are formed in two bands around $\delta\beta^{(+)} \sim \pi$ and $\delta\beta^{(-)} \sim \pi$, as well as in a wider region where both mismatches are positive. Figure 2(c) illustrates FF and SH propagation for $\delta\beta^{(+)} = \pi$ [and $\delta\beta^{(-)} = \pi$, after inversion of the ξ axis] where the FF + FF \rightarrow SH $^{(+)}$ [FF + FF \rightarrow SH $^{(-)}$] interaction prevails, with a net positive [negative] lateral shift of the spatial soliton due to the pulling from the relevant SH component.

These simulations provide useful guidelines for experiments in our HexLN waveguide as the three main control parameters available in the experiments, namely, the FF launch peak power (P_ω), wavelength (λ_ω), and propagation angle (θ_ω), are directly related to $\delta\beta^{(+)}$, $\delta\beta^{(-)}$, and $\gamma^{(\pm)} \propto \sqrt{P_\omega}$. The HexLN waveguide is mounted on a piezoelectrically controlled stage, stabilized at $\sim 85^\circ\text{C}$ to prevent photorefractive damage. The NPL is excited at FF in the range 1.1–1.6 μm by 20 ps (FWHM) narrow linewidth ($< 2\text{ cm}^{-1}$) pulses delivered by an optical parametric generator operating at 10 Hz. The angle θ_ω is adjusted by rotating the sample around its optic axis z , while the FF input is shaped into a cylindrical Gaussian spot (lateral and vertical waists $w_0 = 27.5\ \mu\text{m}$ and $v_0 = 3.4\ \mu\text{m}$, respectively) and end-fire coupled to launch the TM_0 mode. Its propagation in the 18 mm long NPL amounts to ~ 5.4 diffraction lengths ($L_D = 3.3\text{ mm}$). At the device output, the FF and SH are monitored by time-gated photodiodes and imaged on Vidicon and CCD, respectively. The output images are then filtered to eliminate background noise and corrected for the camera gamma-factor (≈ 0.7). The relevant FF output parameters, namely, spot-size (w_{out}) and displacement (Δx), are extracted via Gaussian best fits of the beam along x .

Figure 3 illustrates the experimental data for asymmetric TB SHG, with $\theta_\omega = 0.58^\circ$, where the 2D lattice exhibits distinct resonances at $\lambda^{(-)} = 1546.5\text{ nm}$ and $\lambda^{(+)} = 1555.7\text{ nm}$. The output FF lateral profile in the linear regime (diffraction) is plotted in Fig. 3(a) (the two arrows indicate the directions in which the FF is pulled by the SHG resonances). Figures 3(b) and 3(c) show the FF output component of the soliton at two pump wavelengths close to $\lambda^{(-)}$ and $\lambda^{(+)}$, respectively. For $\lambda^{(-)} \leq \lambda_\omega < \lambda^{(+)}$ [i.e., $\delta\beta^{(-)} \approx \pi$ and $\delta\beta^{(+)} < 0$] the confinement stems from the SH $^{(-)}$ resonance, which shifts the soliton toward negative x . For $\lambda_\omega \geq \lambda^{(+)}$ [i.e., $\delta\beta^{(-)} > \delta\beta^{(+)} \approx \pi$], conversely, the SS is shifted toward positive x due to the dominant

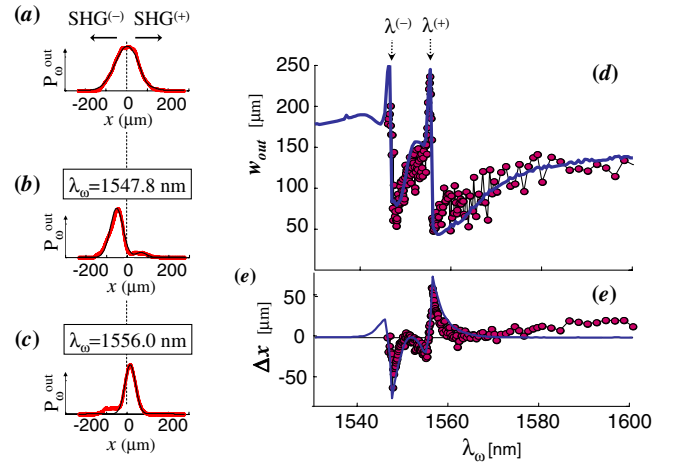


FIG. 3 (color online). Asymmetric TB SHG, with $\theta_\omega = 0.58^\circ$, $\lambda^{(-)} = 1546.5\text{ nm}$, $\lambda^{(+)} = 1555.7\text{ nm}$. FF output beam profiles along x at (a) low and (b),(c) high excitations (peak powers: $P_\omega = 0.5\text{ kW}$ and 22 kW , respectively). (b) $\lambda_\omega = 1547.8\text{ nm}$ and (c) $\lambda_\omega = 1556.0\text{ nm}$. The thin lines are Gaussian fits. Evolution of the FF output (d) beam waist (w_{out}) and (e) lateral displacement (Δx) versus pump wavelength. Measurements (averaged over 100 samples) at $P_\omega = 22\text{ kW}$ (dots) and simulations for $\gamma^{(\pm)} = 4$ (pulsed regime) exhibit lowest output waists slightly larger than the input.

SH $^{(+)}$. The full soliton response versus λ_ω is presented in Figs. 3(d) and 3(e) with good agreement between data (circles) and numerical predictions (solid lines), the latter based on the integration of Eqs. (6) with parameters extracted from the experimental conditions. In Fig. 3(d) the two spectral regions close to $\lambda^{(-)}$ or $\lambda^{(+)}$ for maximum self-confinement are apparent. As discussed with reference to Figs. 3(b) and 3(c), the corresponding lateral shift of the soliton is either negative or positive [Fig. 3(e)], depending on the prevailing SHG process. Therefore, the doubly resonant 2D NPL in the asymmetric configuration entails an entirely new approach to soliton steering not available by conventional singly resonant SHG.

Figure 4 displays the TB SHG soliton response for $\theta_\omega \rightarrow 0$, i.e., the nearly symmetric case when $\lambda^{(\pm)} \rightarrow \lambda_0 = 1551.1\text{ nm}$. Figures 4(a)–4(e) plot the acquired FF component of the output beam for increasing powers at $\lambda_\omega = 1553.0\text{ nm}$, where $\delta\beta^{(\pm)} \sim \pi$. The competing action of the two SHG processes, both close to resonance, yields an interesting dynamics as the excitation is increased well into the soliton regime ($P_\omega \geq 20\text{ kW}$). The harmonics are initially confined and displaced toward $x > 0$ [Fig. 4(b)]; then the beam develops a second hump in $x < 0$ [Fig. 4(c)], until it eventually returns to being singly humped with a shift toward $x < 0$ [Fig. 4(d)]. Finally, for $P_\omega \approx 60\text{ kW}$ the output stabilizes around $x = 0$ [Fig. 4(e)]. Although this behavior is not entirely stationary as both simulations and data show residual breathing and transverse dynamics of the self-confined beam (due to the combined SHG reso-

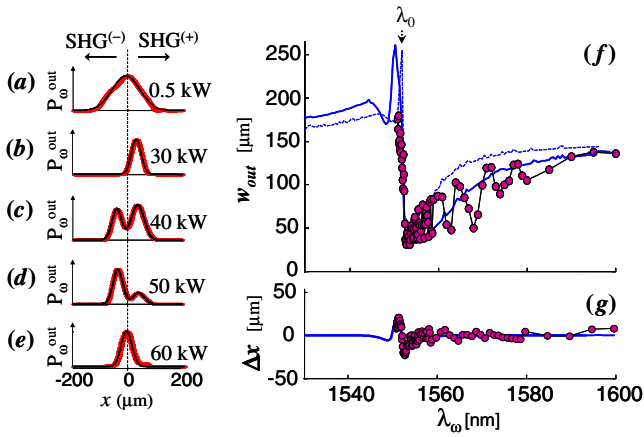


FIG. 4 (color online). Nearly symmetric TB SHG: $\theta_\omega \rightarrow 0^\circ$ and $\lambda^{(-)} \rightarrow \lambda^{(+)} \rightarrow \lambda_0 = 1551.1$ nm. (a–e) FF output beam profiles at $\lambda_\omega = 1553.0$ nm, for peak excitations $P_\omega = 0.5, 30, 40, 50,$ and 60 kW (external powers), respectively. (f) Evolution of the FF output (w_{out}) and (g) lateral displacement (Δx) versus λ_ω ; data for $P_\omega = 25$ kW (dots) and simulations for $\gamma^{(\pm)} = 4$ and $\theta_\omega = 0.05^\circ$. The dashed line refers to singly resonant SHG.

nances), control of the SS profile and its displacement is available by acting on λ_ω and P_ω . The wavelength response in the nearly symmetric configuration for high enough excitations is presented in Figs. 4(f) and 4(g). Since $\lambda^{(\pm)} \rightarrow \lambda_0$, the $w_{\text{out}}-\lambda_\omega$ characteristic exhibits a single dip after λ_0 , corresponding to the formation of an SS for $\delta\beta^{(\pm)} \sim \pi$ [31]. While this resembles the behavior of quadratic solitons via singly resonant SHG, a comparison at equal power levels [Fig. 4(f), dashed line] reveals a broader wavelength interval for self-trapping, stemming from the synergetic action of the two SHG processes.

In conclusion, we presented the first results on parametric spatial solitons in a 2D purely nonlinear lattice. The higher dimensionality allows to map two concurrent SHG processes into the spatial-spectral domains [31]; experiments in planar NPL in LiNbO₃ buried waveguides encompass a wealth of wave dynamics, including SS steering by wavelength, angle, and power. Further investigations will address higher-order resonances, quasicrystals [32], and (multi-) stability.

K. G. acknowledges support from the Leverhulme Trust (No. SRF/40112) and INTAS (No. RG 03-51-6562). We thank the Italian Ministry for University and Research (No. PRIN 2005098337) for partial funding and D. Ostrowsky, A. Boardman, and L. Colace for enlightening discussions.

*assanto@uniroma3.it

[1] H. Feddersen, Phys. Lett. A **154**, 391 (1991).

- [2] A.J. Sievers and S. Takeno, Phys. Rev. Lett. **61**, 970 (1988).
- [3] R. Balakrishnan and A. R. Bishop, Phys. Rev. Lett. **55**, 537 (1985).
- [4] A. Trombettoni and A. Smerzi, Phys. Rev. Lett. **86**, 2353 (2001).
- [5] A.W. Snyder and D.J. Mitchell, Science **276**, 1538 (1997); G.I. Stegeman and M. Segev, Science **286**, 1518 (1999).
- [6] Y. S. Kivshar and G. P. Agrawal, *Optical Solitons: from Fibers to Photonic Crystals* (Academic, New York, 2003); C. Conti and G. Assanto, in *Encyclopedia of Modern Optics*, edited by R.D. Guenther, D.G. Steel, and L. Bayvel (Elsevier, Oxford, 2004), Vol. 5, p. 43.
- [7] D.N. Christodoulides and R.J. Joseph, Opt. Lett. **13**, 794 (1988); D.N. Christodoulides, F. Lederer, and Y. Silberberg, Nature (London) **424**, 817 (2003).
- [8] J.W. Fleisher, M. Segev, N.K. Efremidis, and D.N. Christodoulides, Nature (London) **422**, 147 (2003).
- [9] A. Fratallocchi *et al.*, Opt. Lett. **29**, 1530 (2004); Opt. Express **13**, 1808 (2005).
- [10] A. A. Sukhorukov, Y. S. Kivshar, H. S. Eisenberg, and Y. Silberberg, IEEE J. Quantum Electron. **39**, 31 (2003).
- [11] R. Iwanow *et al.*, Phys. Rev. Lett. **93**, 113902 (2004).
- [12] W. Krolikowski and Y. S. Kivshar, J. Opt. Soc. Am. B **13**, 876 (1996).
- [13] N. K. Efremidis *et al.*, Phys. Rev. Lett. **91**, 213906 (2003).
- [14] T. Pertsch *et al.*, Phys. Rev. Lett. **93**, 053901 (2004).
- [15] N. Akozbek and S. John, Phys. Rev. E **57**, 2287 (1998).
- [16] E. A. Ostrowskaya and Y. S. Kivshar, Opt. Express **12**, 19 (2004), and references therein.
- [17] M. M. Fejer, G. A. Magel, D. H. Jundt, and R. L. Byer, IEEE J. Quantum Electron. **28**, 2631 (1992).
- [18] M. Yamada, N. Nada, M. Saitoh, and K. Watanabe, Appl. Phys. Lett. **62**, 435 (1993).
- [19] V. Berger, Phys. Rev. Lett. **81**, 4136 (1998).
- [20] N. G. R. Broderick *et al.*, Phys. Rev. Lett. **84**, 4345 (2000).
- [21] M. J. Werner and P. D. Drummond, J. Opt. Soc. Am. B **10**, 2390 (1993).
- [22] G. Assanto and G. I. Stegeman, Opt. Express **10**, 388 (2002).
- [23] W. E. Torruellas *et al.*, Phys. Rev. Lett. **74**, 5036 (1995); R. Schiek, Y. Baek, and G. I. Stegeman, Phys. Rev. E **53**, 1138 (1996).
- [24] Y. N. Karamzin and A. P. Sukhorukov, Sov. Phys. JETP **41**, 414 (1976).
- [25] A. V. Buryak, Y. S. Kivshar, and S. Trillo, Phys. Rev. Lett. **77**, 5210 (1996).
- [26] B. Bourliaguet *et al.*, Opt. Lett. **24**, 1410 (1999); R. Schiek *et al.*, Opt. Lett. **29**, 596 (2004); G. Leo *et al.*, Opt. Lett. **29**, 1778 (2004).
- [27] K. Gallo *et al.*, Opt. Lett. **31**, 1232 (2006).
- [28] L. Torner, D. Mazilu, and D. Mihalache, Phys. Rev. Lett. **77**, 2455 (1996).
- [29] W. E. Torruellas *et al.*, Appl. Phys. Lett. **68**, 1449 (1996).
- [30] R. Schiek, Y. Baek, G. I. Stegeman, and W. Sohler, Opt. Lett. **24**, 83 (1999).
- [31] K. Gallo and G. Assanto, Opt. Lett. **32**, 3149 (2007).
- [32] K. Gallo, C. B. E. Gawith, and P. G. R. Smith, Ferroelectrics **340**, 69 (2006).